Ultrafast Carrier Dynamics in 2D $NbTe_2$ Thin Films

David J. Moss

[1]*Optical Sciences Centre, Swinburne University of Technology, Hawthorn, VIC 3122, Australia*

Abstract

As one of the representatives of emerging metallic transition metal dichalcogenides, niobium ditelluride ($NbTe_2$) has attracted intensive interest recently due to its distorted lattice structure and unique physical properties. Here, we report on the ultrafast carrier dynamics in $NbTe_2$ measured using time-resolved pump-probe transient reflection spectroscopy. A thickness-dependent carrier relaxation time is observed, exhibiting a clear increase in the fast and slow carrier decay rates for thin $NbTe_2$ flakes. In addition, pump power dependent measurements indicate that the carrier relaxation rates are power-independent, with the peak amplitude of the transient reflectivity increasing linearly with pump power. Isotropic relaxation dynamics in $NbTe_2$ is also verified by performing polarization-resolved pump-probe measurements. These results provide an insight into the light-matter interactions and charge carrier dynamics in $NbTe_2$ and will pave the way for its applications to photonic and optoelectronic devices.

KEYWORDS: Layered transition metal dichalcogenides, $NbTe_2$ flake, ultrafast carrier dynamics, pump-probe spectroscopy.

1. INTRODUCTION

Since the ground-breaking discovery of graphene,[1] two-dimensional (2D) layered materials have undergone a tremendous surge in interest in the past decade, both in fundamental science as well as industrial applications.[2-8] Layered transition metal dichalcogenides (TMDCs), with a formula of MX_2 (M represents transition metal and X is chalcogen element), are a widely studied family of 2D materials that have demonstrated huge potential for electronic and optical devices owing to their novel electrical and optical properties. Thanks to their atomic film thickness and high carrier mobilities, monolayer MoS_2 and WeS_2 films have been used for sub-5nm field-effect transistors (FETs).[9-11] A layer-tunable optical band gap that covers a spectral range from the visible to the NIR regions makes TMDCs promising for broadband photodetectors and highly efficient solar cells.[12-14] In addition, strong light-matter interactions in atomically thin $MoSe_2$, WS_2, and $PdSe_2$ above their bandgap gives rise to many fascinating phenomena, such as exotic excitonic properties,[15-17] a strong optical nonlinearity,[18-19] and quantum interference,[20-21] enabling many new photonic and quantum devices.

Recently, metallic 1-*T* phase TMDCs with exotic physical properties, such charge density waves (CDW) and low-temperature superconductivity, have attracted significant interest.[22-28] $NbTe_2$ is one example that is a semimetal with a topologically protected band crossing.[29] Owing to its semimetal nature and ultrahigh electrical conductivity, $NbTe_2$ has been used as conductive electrode to reduce the contact resistance and improve carrier mobility of other 2D semiconductors.[24-25] More importantly, $NbTe_2$ exhibits a coexistence of CDW and superconductivity below 0.74 K, providing a good platform for unconventional superconductivity and strongly correlated electron systems.[26-28] Linear magnetoresistance and anisotropic magneto-transport properties were also experimentally observed, demonstrating its strong potential for magnetic devices.[27, 30] Although progress has been promising for electric and magnetic applications, the optical properties of $NbTe_2$ have yet to be investigated. This includes the ultrafast carrier dynamics and layer-dependent light-matter interaction.

In this work, we characterize the photon-excited carrier dynamics in mechanically exfoliated $NbTe_2$ flakes having thicknesses from ~ 15 – 50 nm via time-resolved transient reflection spectroscopy. Photoinduced bleaching (PB) of 1040 nm probe light is experimentally achieved when the samples are irradiated by a pump at 520 nm. Thickness-dependent carrier relaxation times are observed, where both the fast and slow relaxation rates decrease with sample thickness. We also observe a linear increase in the transient reflection peak amplitude with pump power, whereas the photon-excited carrier decay times are power independent. In addition, polarization-resolved Raman and pump-probe measurements show that the relaxation dynamics are isotropic. Our results present a comprehensive analysis of photon-excited carrier dynamics in $NbTe_2$ and provide guidance for its applications to photonic and optoelectronic devices.

2. MATERIALS AND CHARACTERIZATION

Sample preparation. $NbTe_2$ single crystals were synthesized by the chemical vapor transport (CVT) technique.[27, 31] High purity Nb foil (99.99%), Te power (99.999%), and iodine (99%) were sealed in an evacuated quartz tube, which was subsequently heated to 550 ℃ and held for one day in a two-zone furnace. After that, the heating temperatures of the two-zone furnace were increased to 850 ℃ (source side) and 750 ℃ (sink side) and kept for one week. After cooled naturally, $NbTe_2$ single crystals were obtained. $NbTe_2$ flakes with different thicknesses were exfoliated from the bulk crystals using adhesive tape and transferred onto quartz substrates.

Material characterization. Morphology images and thicknesses of the samples were characterized using atomic force microscopy (Alpha 300ras, WITec) in tapping mode. The resolutions in vertical and transverse directions were ~ 0.1 nm and ~ 8 nm, respectively. Raman spectra were characterized with the same instrument with a 532 nm laser excitation. The linear absorbance of the materials was measured by an ultraviolet-visible (UV-vis) spectrometer.

Time-resolved pump-probe technique. The transient reflection measurements were performed using a Yb fiber-based laser (Menlo Systems) with a central wavelength at 1040 nm. The repetition rate and pulse width of the laser were 100 MHz and 150 fs, respectively. The laser beam size is ~ 4 μm. Five percent of the output laser was employed as a probe beam while the balance of 95% provided the pump pulse at 520 nm via frequency doubling. A half-wave plate combined with a linear polarizer was used as a continuously adjustable power attenuator. After passing through a free space time–delay line, the pump and probe pulses were focused with an objective lens (Tu Plan Fluor 50 x NA = 0.8, Nikon) onto the sample surface with a Gaussian spot. The reflected probe beam was separated from the pump light by using a color filter before reaching the silicon photodetector, which significantly improved the signal-to-noise ratio. A lock-in amplifier (SR865A, Stanford Research Systems) referenced to 1.5 kHz mechanically chopped pump (SR542, Stanford Research Systems) was employed to collect the reflection change (ΔR) of the probe beam due to the pump excitation.

3. RESULTS AND DISCUSSION

$NbTe_2$ is a typical layered CDW material with two different structural phases. At high temperature (above 550 K), it exhibits a high symmetry 1-*T* phase where each Nb atom is coordinated octahedrally by Te atoms.[32] Below 550 K, $NbTe_2$ undergoes a CDW phase transition which results in a displacement of Nb atoms from the octahedral centers to a monoclinically distorted 1-*T* phase (1-*T′* phase).[28, 30] This 1-*T′* phase is very stable at room temperature since the phase transition temperature is much higher. The crystal structure of 1-*T′* $NbTe_2$ is shown in Figure 1(a).

Each monolayer is composed of an Nb layer sandwiched by two Te layers, where the Nb atoms are displaced within the plane to form "trimers," whereas the Te atoms present an out-of-plane buckling.[28, 32] The Te-Nb-Te sandwiches stack with weak van der Waals interactions to form a layered structure.

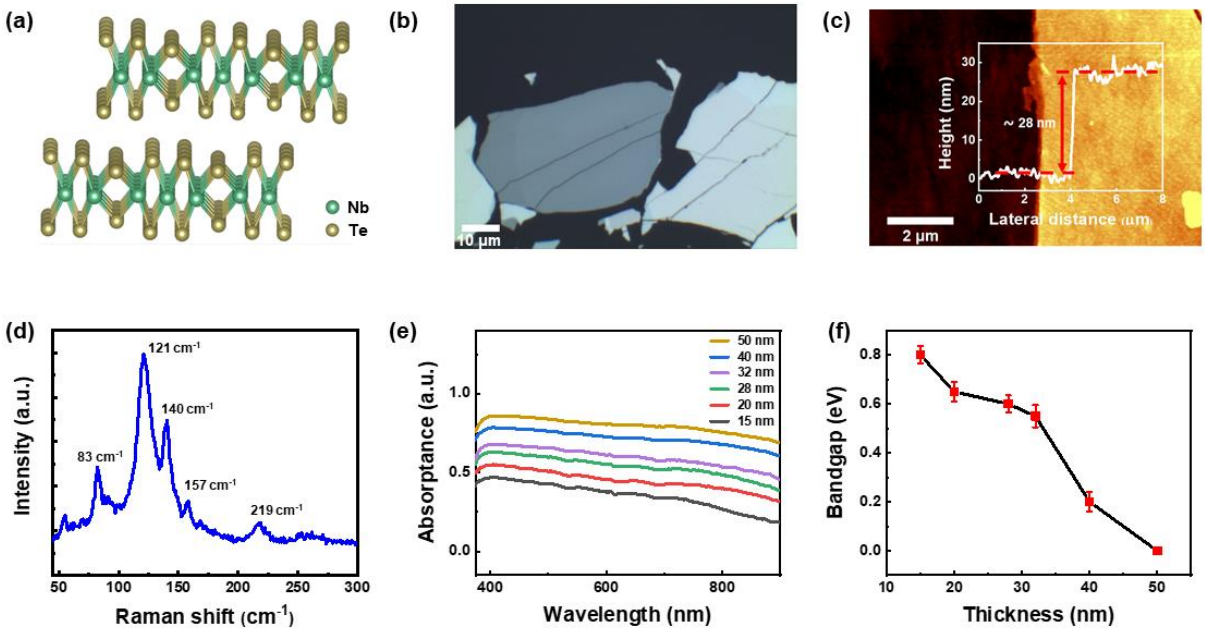

Figure 1. (a) Schematic crystal structure of monoclinic 1-*T′* $NbTe_2$. The green and yellow dots represent the Nb and Te atoms, respectively. (b) Optical microscopy image of an exfoliated $NbTe_2$ flake. (c) AFM height profile of the $NbTe_2$ flake. The measured thickness is ~ 28 nm. (d) Raman spectrum excited via a 532 nm laser. (e) UV-vis absorption spectrum. (f) Determined optical bandgaps of samples with different thicknesses.

We prepared single crystal $NbTe_2$ flakes with different thicknesses via mechanical exfoliation. An optical microscopy image of a representative sample is shown in Figure 1(b). Different contrasts represent areas with different thicknesses. It can be seen that the exfoliated flake presents a flat surface with uniform thickness in the different areas. Figure 1(c) shows the AFM height profile of the $NbTe_2$ flake, which indicates that the thickness of the flake is ~ 28 nm. Due to the strong interlayer coupling of $NbTe_2$, it is very difficult to obtain very thin samples using mechanical exfoliation.[25] The thinnest flake obtained in our experiments is ~ 15 nm. Further AFM images of $NbTe_2$ flakes with different thickness are shown in Figure S2 (Supporting Information). The Raman spectrum of a $NbTe_2$ flake is shown in Figure 1(d) with an excitation laser at 532 nm. Characteristic peaks at ~55 cm^{-1}, ~83 cm^{-1}, ~121 cm^{-1}, ~140 cm^{-1}, ~157 cm^{-1}, ~168 cm^{-1}, ~219 cm^{-1}, and ~262 cm^{-1} can be observed, which correspond to the phonon modes of A_g^1, A_g^2, A_g^4, A_g^5, A_g^6, B_g^4, A_g^7, and A_g^8 in $NbTe_2$, respectively.[33-34] These results indicate the high crystal quality of the samples. Optical absorption spectra (from 400 nm to 900 nm) of $NbTe_2$ flakes with different thicknesses were measured by using a UV-vis spectrometer, as shown in Figure 1(e). A broadband absorption response with a smooth absorption band in the wavelength range can be observed for all the thicknesses. The thickness-dependent optical bandgap is estimated from a Tauc plot of $(\alpha h\nu)^{1/2}$ versus $h\nu$ based on the Tauc formula (Figure S3), where α and $h\nu$ represent the optical absorption coefficient and photon energy, respectively. Figure 1(f) shows the measured optical bandgaps as a function of thicknesses, where the bandgap of the $NbTe_2$ decreases from ~ 0.8 eV to 0 eV with increasing the sample thickness from 15 nm to 50 nm.

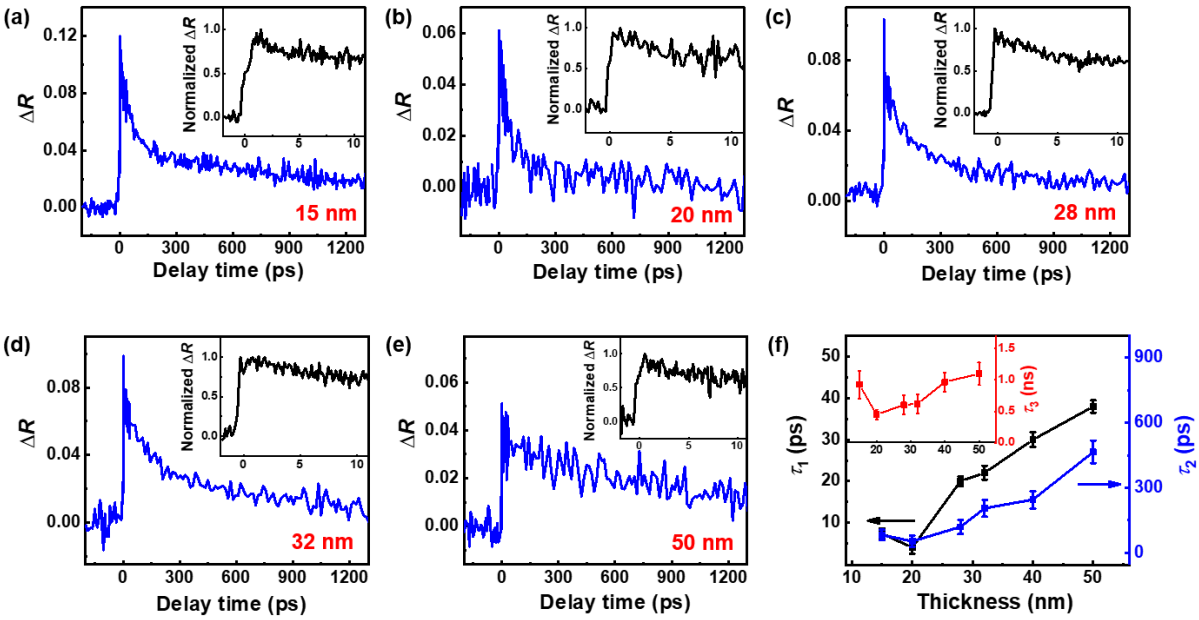

Figure 2. (a)–(e) Time-resolved transient reflection (Δ*R*) curves of $NbTe_2$ flakes with different thicknesses. The laser powers of pump (520 nm) and probe (1040 nm) beams are ~ 40 μW and ~ 35 μW, respectively. The insets show the normalized Δ*R* curves around 0 delay time. (f) The measured relaxation time constants with different thicknesses.

To characterize the photon-excited carrier dynamics, time-resolved pump-probe transient reflection (Δ*R*) spectroscopy was used with a pump laser at 520 nm and probe laser at 1040 nm. The pump-induced probe reflection change ($\Delta R=R-R_0$) was measured by chopping the pump and monitoring the output of the photodiode with a lock-in amplifier, where R and R_0 are the probe reflections with and without pump light, respectively. Figures 2(a) – (e) show the time-resolved Δ*R* curves for flakes with thicknesses from ~15 nm to ~50 nm. The insets of these figures present the corresponding normalized Δ*R* curves for 0 delay times. It can be seen that, for all thicknesses, a fast increase of probe reflection from zero to its maximum value (positive ΔR) is observed at zero-delay. The positive ΔR indicates photoinduced bleaching (PB) of the probe light.[35] Since the $NbTe_2$ bandgap is much less than the pump photon energy (~2.38 eV), the pump can excite electrons directly from the valance to conduction bands. These excited carriers are commonly known to decrease the absorption of the probe light and enhance its reflection due to the filling of states and the Pauli-blocking effect.[36-39]

After Δ*R* reaches its maximum, a decay process can be observed in the Δ*R* curves, which can be mainly separated into two components: a sharp drop of ΔR followed by a slow relaxation process, as shown in Figure 2(a) – (e). By fitting the experimental data, relaxation time constants during the decay process can be obtained. In our case, a tri-exponential decay function was used to fit the measured Δ*R* curves, as follows:[40-41]

$$\frac{\Delta R(t)}{R_0} = A\exp\left(\frac{-t}{\tau_1}\right) + B\exp\left(\frac{-t}{\tau_2}\right) + C\exp\left(\frac{-t}{\tau_3}\right) \quad (1)$$

where *A*, *B*, and *C* denote the corresponding amplitudes. *t* denotes the delay time between the pump and probe, and τ_1, τ_2, and τ_3 are the time constants of relaxation processes. Here, we combine the semi-log fit with the tri-exponential fit for better evaluation of the time constants.

The measured values of τ_1, τ_2, and τ_3 for different film thicknesses are presented in Figure 2(f). It can be seen that the sample having the fastest relaxation time was 15-nm thick, and had a $\tau_1 \sim 7.4$ ps. This is in the same order of magnitude of other TMDCs, such as MoS_2[42-43] and $PdSe_2$.[35] This picosecond relaxation process can be attributed to carrier–carrier and carrier–phonon scattering during the carrier-cooling process.[44-47] The pump-excited hot carriers initially thermalize to quasi-equilibrium states through carrier-carrier scattering. They then transfer their energy to the $NbTe_2$ lattice and are cooled mainly by electron–phonon scattering. A thickness-dependent behavior can be observed in τ_1, where it increases from ~ 7.4 ps to 38.3 ps as the sample thickness increases from 15 nm to 50 nm. It has been demonstrated that an increase in thickness in TMDCs can lead to an enhancement of dielectric screening of the long-range Coulomb interaction, weakening the electron–phonon coupling,[48-49] which in turn increases the relaxation time τ_1 for thicker samples.

The time constant τ_2 exhibits a similar trend to τ_1 with increasing sample thickness, although with an overall slower lifetime, ranging from ~ 83.4 ps for 15-nm to ~ 465 ps for the 50-nm flakes, as shown in Figure 2(f). We attribute this relatively longer relaxation process to the anharmonicity-driven phonon-phonon scattering.[50] As discussed above, τ_1 denotes carrier relaxation to phonons via fast carrier-phonon scattering processes. The subsequent thermalization of these generated phonons with the rest of the phonon subsystem takes a longer time via the anharmonicity-driven phonon-phonon scattering. This phonon dominating process may also explain the thickness-dependent τ_2 because of the slower phonon cooling process occurring in thicker flakes.[51] The longest lifetime τ_3, is on a nanosecond time scale (inset of Figure 2(f)), which arises from lattice cooling by dissipating the energy to the substrate.[37, 52-53]

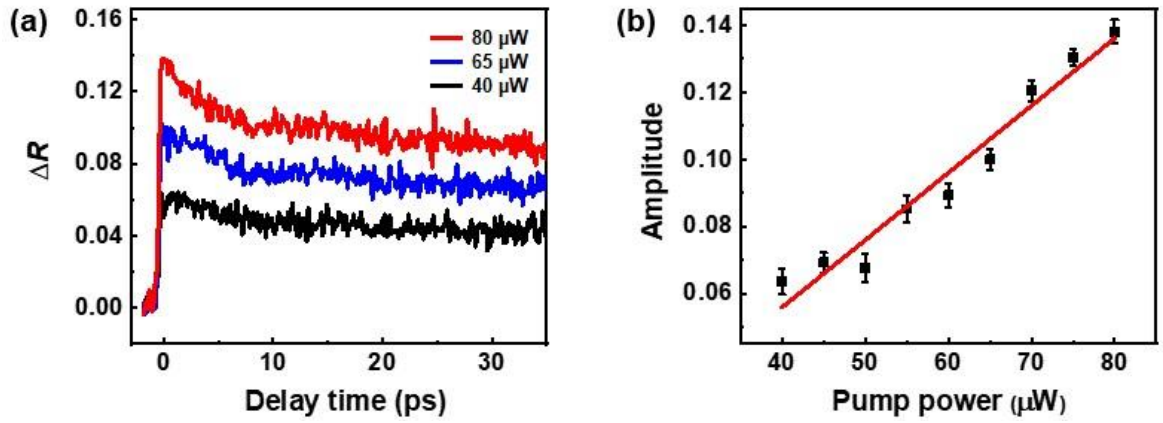

Figure 3. (a) Time-resolved transient reflection (ΔR) curves of a 32 nm-$NbTe_2$ flake with different pump laser powers. (b) Corresponding peak amplitudes of the ΔR curves as a function of the pump power. The black solid squares represent the experimental data, and the red solid line is the linear fit.

Figures 3(a) shows pump power dependent ΔR measurements for a 32 nm-flake with pump powers from 40 μW to 80 μW, with the probe power fixed at 35 μW. Similar temporal features in the ΔR curves can be observed for different pump powers, indicating that the carrier relaxation dynamics in $NbTe_2$ are pump power independent, similar to other TMDCs.[43, 46] In contrast, for the ΔR amplitudes, a clear increase with pump power is observed. Figure 3(b) plots the corresponding peak amplitudes extracted from the ΔR curves in Figure 3(a), demonstrating a linear relationship between the amplitude and pump power. The observed linear contribution of the pump power indicates a one-photon excitation of carriers in $NbTe_2$ with the pump beam and contribution to Pauling blocking

at the probe wavelength.[35, 43] The extracted peak amplitudes as a functions of pump power for other thicknesses are presented in Figure S4.

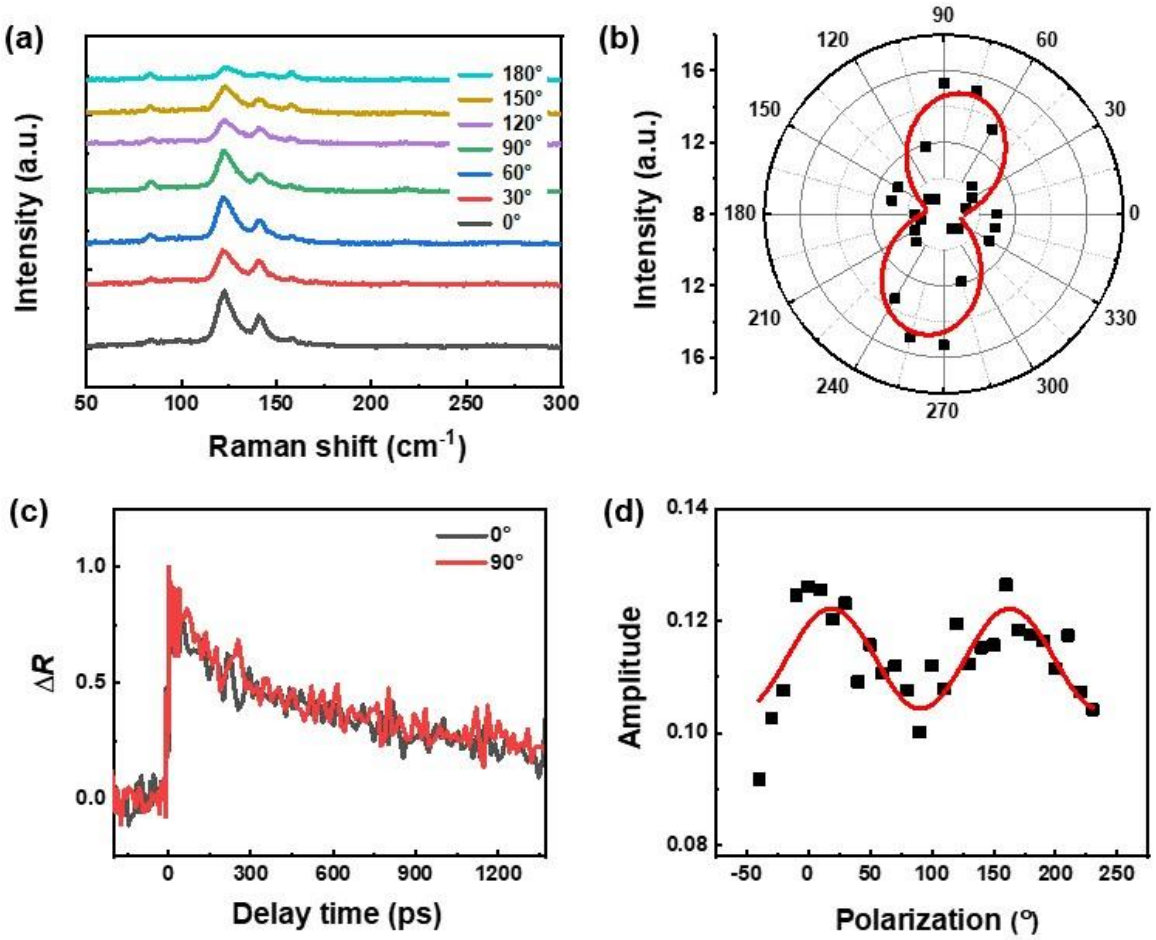

Figure 4. (a) Polarization-dependent Raman spectra of $NbTe_2$ flake. (b) Polarization diagram of the Raman intensities of A_g^2 mode (~ 83.4 cm^{-1}) was extracted through the fitting of the Raman spectra of each polarization angle under the parallel configurations. (c) Normalized Δ*R* curves under different pump polarization, where the probe polarization is fixed at 0°. (d) Peak amplitudes as a function of pump polarization angles with respect to the sample orientation.

We investigated the anisotropic ultrafast carrier dynamics via polarization-dependent pump-probe measurements. Angle-resolved polarized Raman spectroscopy was used to analyze the crystal axis of $NbTe_2$ flakes under a parallel configuration, with an excitation laser wavelength of 532 nm. In the experiment, we fixed the sample and rotated the polarizers in the incident and scattered light paths to vary the angle between the sample crystallographic orientation and the polarizations of beams. Figure 4(a) shows the Raman spectra of a flake for different excitation laser polarization angles. To better illustrate the polarization trend, the polarization diagram of A_g^2 mode of the sample is plot in Figure 4(b). It can be seen that the peak intensity of the Ag mode oscillates with a periodicity of 180° as the orientation of the polarization is rotated. Therefore, by using this polarization diagram, the crystallographic orientation of the flakes can easily be determined.

After determining the crystal directions, we conducted the polarization-resolved pump-probe measurements. The pump and probe powers were 40 and 35 μW, respectively, with their polarization angles controlled by rotating

a half-wave plate. Figure 4(c) shows the normalized ΔR curves of the 40-nm sample for pump polarization angles of 0° and 90° with respect to the sample orientation. Varying the pump polarization did not change their temporal response, indicating that the photon-excited carrier relaxation process is isotropic in $NbTe_2$ flake. We also measured the peak amplitudes of the ΔR curves under different pump polarization angles (Figure 4(d)) where a sinusoidal dependence on the polarization angles is observed, originating mainly from the anisotropic pump absorption. This is further verified by the polarization-dependent transmission of pump light in the sample, as shown in Figure S5.

4. CONCLUSIONS

In summary, by using time-resolved transient reflection spectroscopy, we characterize the photon-excited carrier dynamics in mechanically exfoliated single crystal $NbTe_2$ flakes. A typical photoinduced bleaching (PB) of probe light at 1040 nm and thickness-dependent relaxation dynamics of excited carriers in $NbTe_2$ flakes are observed when the samples are irradiated with a 520-nm pump beam. The influence of the pump power is also investigated, showing a linear increase in the transient reflection peak amplitude with pump power, with a power-independent carrier decay. Polarization-resolved pump-probe measurements indicate that the carrier relaxation dynamics in $NbTe_2$ is isotropic. These properties demonstrate the potential of $NbTe_2$ as a novel and interesting 2D material for photonic and optoelectronic applications. In particular, these results indicate that the ultrafast response of single crystal $NbTe_2$ flakes could be useful for integrated photonic chips based on CMOS compatible platforms for microcomb devices [55-70] for high bandwidth applications [71-190].

REFERENCES

1. Novoselov, K. S.; Geim, A. K.; Morozov, S. V.; Jiang, D.; Zhang, Y.; Dubonos, S. V.; Grigorieva, I. V.; Firsov, A. A., Electric Field Effect in Atomically Thin Carbon Films. *Science* **2004,** *306* (5696), 666.
2. Sun, Z.; Martinez, A.; Wang, F., Optical modulators with 2D layered materials. *Nat. Photonics* **2016,** *10* (4), 227-238.
3. Wu, J.; Jia, L.; Zhang, Y.; Qu, Y.; Jia, B.; Moss, D. J., Graphene Oxide for Integrated Photonics and Flat Optics. *Adv. Mater.* **2021,** *33* (3), 2006415.
4. Liu, Y.; Duan, X.; Shin, H. J.; Park, S.; Huang, Y.; Duan, X., Promises and prospects of two-dimensional transistors. *Nature* **2021,** *591* (7848), 43-53.
5. Wu, J.; Yang, Y.; Qu, Y.; Jia, L.; Zhang, Y.; Xu, X.; Chu, S. T.; Little, B. E.; Morandotti, R.; Jia, B.; Moss, D. J., 2D Layered Graphene Oxide Films Integrated with Micro-Ring Resonators for Enhanced Nonlinear Optics. *Small* **2020,** *16* (16), e1906563.
6. Wu, J.; Yang, Y.; Qu, Y.; Xu, X.; Liang, Y.; Chu, S. T.; Little, B. E.; Morandotti, R.; Jia, B.; Moss, D. J., Graphene Oxide Waveguide and Micro-Ring Resonator Polarizers. *Laser Photonics Rev.* **2019,** *13* (9), 1900056.
7. Qu, Y.; Wu, J.; Yang, Y.; Zhang, Y.; Liang, Y.; El Dirani, H.; Crochemore, R.; Demongodin, P.; Sciancalepore, C.; Grillet, C.; Monat, C.; Jia, B.; Moss, D. J., Enhanced Four‐Wave Mixing in Silicon Nitride Waveguides Integrated with 2D Layered Graphene Oxide Films. *Adv. Opt. Mater.* **2020,** *8* (23), 2001048.
8. Yang, Y.; Wu, J.; Xu, X.; Liang, Y.; Chu, S. T.; Little, B. E.; Morandotti, R.; Jia, B.; Moss, D. J., Enhanced four-wave mixing in waveguides integrated with graphene oxide. *APL Photonics* **2018,** *3* (12), 120803.
9. Fang, H.; Chuang, S.; Chang, T. C.; Takei, K.; Takahashi, T.; Javey, A., High performance single layered WSe_2 p-FETs with chemically doped contacts. *Nano Lett.* **2012,** *12* (7), 3788-92.
10. Radisavljevic, B.; Radenovic, A.; Brivio, J.; Giacometti, V.; Kis, A., Single-layer MoS2 transistors. *Nat. Nanotechnol.* **2011,** *6* (3), 147-50.
11. Sebastian, A.; Pendurthi, R.; Choudhury, T. H.; Redwing, J. M.; Das, S., Benchmarking monolayer MoS2 and WS2 field-effect transistors. *Nat. Commun.* **2021,** *12* (1), 693.
12. Liang, Q.; Wang, Q.; Zhang, Q.; Wei, J.; Lim, S. X.; Zhu, R.; Hu, J.; Wei, W.; Lee, C.; Sow, C.; Zhang, W.; Wee, A. T. S., High-Performance, Room Temperature, Ultra-Broadband Photodetectors Based on Air-Stable PdSe2. *Adv. Mater.* **2019,** *31* (24), e1807609.
13. McVay, E.; Zubair, A.; Lin, Y.; Nourbakhsh, A.; Palacios, T., Impact of Al2O3 Passivation on the Photovoltaic Performance of Vertical WSe2 Schottky Junction Solar Cells. *ACS Appl. Mater. Interfaces* **2020,** *12* (52), 57987-57995.
14. Jia, L.; Wu, J.; Zhang, Y.; Qu, Y.; Jia, B.; Chen, Z.; Moss, D. J., Fabrication Technologies for the On‐Chip Integration of 2D Materials. *Small Methods* **2022,** *6* (3), 2101435.
15. Wang, Z.; Rhodes, D. A.; Watanabe, K.; Taniguchi, T.; Hone, J. C.; Shan, J.; Mak, K. F., Evidence of high-temperature exciton condensation in two-dimensional atomic double layers. *Nature* **2019,** *574* (7776), 76-80.
16. Yu, Y.; Yu, Y.; Li, G.; Puretzky, A. A.; Geohegan, D. B.; Cao, L., Giant enhancement of exciton diffusivity in two-dimensional semiconductors. *Sci. Adv.* **2020,** *6* (51), eabb4823.
17. Conway, M. A.; Muir, J. B.; Earl, S. K.; Wurdack, M.; Mishra, R.; Tollerud, J. O.; Davis, J. A., Direct measurement of biexcitons in monolayer WS2. *2D Mater.* **2022,** *9* (2), 021001.
18. Trovatello, C.; Marini, A.; Xu, X.; Lee, C.; Liu, F.; Curreli, N.; Manzoni, C.; Dal Conte, S.; Yao, K.; Ciattoni, A.; Hone, J.; Zhu, X.; Schuck, P. J.; Cerullo, G., Optical parametric amplification by monolayer transition metal dichalcogenides. *Nat. Photonics* **2020,** *15* (1), 6-10.
19. Jia, L. N.; Wu, J. Y.; Yang, T. S.; Jia, B. H.; Moss, D. J., Large Third-Order Optical Kerr Nonlinearity in Nanometer-Thick PdSe2 2D Dichalcogenide Films: Implications for Nonlinear Photonic Devices. *ACS Appl. Nano Mater.* **2020,** *3* (7), 6876-6883.

20. He, Y. M.; Clark, G.; Schaibley, J. R.; He, Y.; Chen, M. C.; Wei, Y. J.; Ding, X.; Zhang, Q.; Yao, W.; Xu, X.; Lu, C. Y.; Pan, J. W., Single quantum emitters in monolayer semiconductors. *Nat. Nanotechnol.* **2015,** *10* (6), 497-502.

21. Chakraborty, C.; Kinnischtzke, L.; Goodfellow, K. M.; Beams, R.; Vamivakas, A. N., Voltage-controlled quantum light from an atomically thin semiconductor. *Nat. Nanotechnol.* **2015,** *10* (6), 507-11.

22. Li, J.; Zhao, B.; Chen, P.; Wu, R.; Li, B.; Xia, Q.; Guo, G.; Luo, J.; Zang, K.; Zhang, Z.; Ma, H.; Sun, G.; Duan, X.; Duan, X., Synthesis of Ultrathin Metallic MTe2 (M = V, Nb, Ta) Single-Crystalline Nanoplates. *Adv. Mater.* **2018**, e1801043.

23. Sugawara, K.; Nakata, Y.; Shimizu, R.; Han, P.; Hitosugi, T.; Sato, T.; Takahashi, T., Unconventional Charge-Density-Wave Transition in Monolayer 1T-TiSe2. *ACS Nano* **2016,** *10* (1), 1341-1345.

24. Wu, R.; Tao, Q.; Dang, W.; Liu, Y.; Li, B.; Li, J.; Zhao, B.; Zhang, Z.; Ma, H.; Sun, G.; Duan, X.; Duan, X., van der Waals Epitaxial Growth of Atomically Thin 2D Metals on Dangling-Bond-Free WSe2 and WS2. *Adv. Funct. Mater.* **2019,** *29* (12), 1806611.

25. Du, M.; Cui, X.; Yoon, H. H.; Das, S.; Uddin, M. D. G.; Du, L.; Li, D.; Sun, Z., Switchable Photoresponse Mechanisms Implemented in Single van der Waals Semiconductor/Metal Heterostructure. *ACS Nano* **2022,** *16* (1), 568-576.

26. Nagata, S.; Abe, T.; Ebisu, S.; Ishihara, Y.; Tsutsumi, K., Superconductivity in the metallic layered compound NbTe2. *J. Phys. Chem. Solids* **1993,** *54* (8), 895-899.

27. Chen, H.; Li, Z.; Fan, X.; Guo, L.; Chen, X., Quantum linear magnetoresistance in NbTe2. *Solid State Commun.* **2018,** *275*, 16-20.

28. Feng, H.; Xu, Z.; Zhuang, J.; Wang, L.; Liu, Y.; Xu, X.; Song, L.; Hao, W.; Du, Y., Role of Charge Density Wave in Monatomic Assembly in Transition Metal Dichalcogenides. *Adv. Funct. Mater.* **2019,** *29* (15), 1900367.

29. Tang, F.; Po, H. C.; Vishwanath, A.; Wan, X., Comprehensive search for topological materials using symmetry indicators. *Nature* **2019,** *566* (7745), 486-489.

30. Gu, S.; Fan, K.; Yang, Y.; Wang, H.; Li, Y.; Qu, F.; Liu, G.; Li, Z.-a.; Wang, Z.; Yao, Y.; Li, J.; Lu, L.; Yang, F., Classical linear magnetoresistance in exfoliated NbTe2 nanoflake. *Phys. Rev. B* **2021,** *104* (11), 115203.

31. Li, Z.; Chen, H.; Jin, S.; Gan, D.; Wang, W.; Guo, L.; Chen, X., Weyl Semimetal TaAs: Crystal Growth, Morphology, and Thermodynamics. *Cryst. Growth Des.* **2016,** *16* (3), 1172-1175.

32. Battaglia, C.; Cercellier, H.; Clerc, F.; Despont, L.; Garnier, M. G.; Koitzsch, C.; Aebi, P.; Berger, H.; Forró, L.; Ambrosch-Draxl, C., Fermi-surface-induced lattice distortion in $NbTe_2$. *Phys. Rev. B* **2005,** *72* (19), 195114.

33. Barajas-Aguilar, A. H.; Irwin, J. C.; Garay-Tapia, A. M.; Schwarz, T.; Paraguay Delgado, F.; Brodersen, P. M.; Prinja, R.; Kherani, N.; Jimenez Sandoval, S. J., Crystalline structure, electronic and lattice-dynamics properties of $NbTe_2$. *Sci. Rep.* **2018,** *8* (1), 16984.

34. Wang, K.; Guo, Z.; Li, Y.; Guo, Y.; Liu, H.; Zhang, W.; Zou, Z.; Zhang, Y.; Liu, Z., Few-Layer $NbTe_2$ Nanosheets as Substrates for Surface-Enhanced Raman Scattering Analysis. *ACS Appl. Nano Mater.* **2020,** *3* (11), 11363-11371.

35. Huo, C.-F.; Wen, R.; Yan, X.-Q.; Li, D.-K.; Huang, K.-X.; Zhu, Y.; Cui, Q.; Xu, C.; Liu, Z.-B.; Tian, J.-G., Thickness-dependent ultrafast charge-carrier dynamics and coherent acoustic phonon oscillations in mechanically exfoliated PdSe2 flakes. *Phys. Chem. Chem. Phys.* **2021,** *23* (36), 20666-20674.

36. Wang, G.; Wang, K.; McEvoy, N.; Bai, Z.; Cullen, C. P.; Murphy, C. N.; McManus, J. B.; Magan, J. J.; Smith, C. M.; Duesberg, G. S.; Kaminer, I.; Wang, J.; Blau, W. J., Ultrafast Carrier Dynamics and Bandgap Renormalization in Layered PtSe2. *Small* **2019,** *15* (34), e1902728.

37. Zhao, X.; Liu, F.; Liu, D.; Yan, X.-Q.; Huo, C.; Hui, W.; Xie, J.; Ye, Q.; Guo, C.; Yao, Y.; Liu, Z.-B.; Tian, J.-G., Thickness-dependent ultrafast nonlinear absorption properties of PtSe2 films with both semiconducting and semimetallic phases. *Appl. Phys. Lett.* **2019,** *115* (26), 263102.

38. Jia, L.; Cui, D.; Wu, J.; Feng, H.; Yang, Y.; Yang, T.; Qu, Y.; Du, Y.; Hao, W.; Jia, B.; Moss, D. J., Highly nonlinear BiOBr nanoflakes for hybrid integrated photonics. *APL Photonics* **2019,** *4* (9), 090802.

39. Zhang, Y.; Wu, J.; Yang, Y.; Qu, Y.; Jia, L.; Moein, T.; Jia, B.; Moss, D. J., Enhanced Kerr Nonlinearity and Nonlinear Figure of Merit in Silicon Nanowires Integrated with 2D Graphene Oxide Films. *ACS Appl. Mater. Interfaces* **2020,** *12* (29), 33094-33103.

40. Kabanov, V. V.; Demsar, J.; Podobnik, B.; Mihailovic, D., Quasiparticle relaxation dynamics in superconductors with different gap structures: Theory and experiments on YBa2Cu3O7-δ. *Phys. Rev. B* **1999,** *59* (2), 1497-1506.

41. Miller, J. K.; Qi, J.; Xu, Y.; Cho, Y. J.; Liu, X.; Furdyna, J. K.; Perakis, I.; Shahbazyan, T. V.; Tolk, N., Near-bandgap wavelength dependence of long-lived traveling coherent longitudinal acoustic phonons in GaSb-GaAs heterostructures. *Phys. Rev. B* **2006,** *74* (11), 113313.

42. Wang, Q.; Ge, S.; Li, X.; Qiu, J.; Ji, Y.; Feng, J.; Sun, D., Valley Carrier Dynamics in Monolayer Molybdenum Disulfide from Helicity-Resolved Ultrafast Pump–Probe Spectroscopy. *ACS Nano* **2013,** *7* (12), 11087-11093.

43. Das, S.; Wang, Y.; Dai, Y.; Li, S.; Sun, Z., Ultrafast transient sub-bandgap absorption of monolayer MoS2. *Light. Sci. Appl.* **2021,** *10* (1), 27.

44. Xu, Y.; Khafizov, M.; Satrapinsky, L.; Kus, P.; Plecenik, A.; Sobolewski, R., Time-resolved photoexcitation of the superconducting two-gap state in MgB2 thin films. *Phys. Rev. Lett.* **2003,** *91* (19), 197004.

45. Taneda, T.; Pepe, G. P.; Parlato, L.; Golubov, A. A.; Sobolewski, R., Time-resolved carrier dynamics and electron-phonon coupling strength in proximized weak ferromagnet-superconductor nanobilayers. *Phys. Rev. B* **2007,** *75* (17), 174507.

46. Li, D.; Fu, J.; Suo, P.; Zhang, W.; Lu, B.; Lin, X.; Yan, X.; Li, B.; Ma, G.; Yao, J., Layer dependent interlayer coherent phonon dynamics in PdSe2 films. *Appl. Phys. Lett.* **2021,** *118* (19), 191105.

47. Nie, Z.; Long, R.; Sun, L.; Huang, C.-C.; Zhang, J.; Xiong, Q.; Hewak, D. W.; Shen, Z.; Prezhdo, O. V.; Loh, Z.-H., Ultrafast Carrier Thermalization and Cooling Dynamics in Few-Layer MoS2. *ACS Nano* **2014,** *8* (10), 10931-10940.

48. Cheiwchanchamnangij, T.; Lambrecht, W. R. L., Quasiparticle band structure calculation of monolayer, bilayer, and bulk MoS2. *Phys. Rev. B* **2012,** *85* (20), 205302.

49. Qiu, W.; Liang, W.; Guo, J.; Fang, L.; Li, N.; Feng, Q.; Luo, S. N., Thickness-dependent ultrafast hot carrier and phonon dynamics of PtSe2 films measured with femtosecond transient optical spectroscopy. *J. Phys. D: Appl. Phys.* **2020,** *54* (7), 075102.

50. Anikin, A.; Schaller, R. D.; Wiederrecht, G. P.; Margine, E. R.; Mazin, I. I.; Karapetrov, G., Ultrafast dynamics in the high-symmetry and in the charge density wave phase of 2H−NbSe2. *Phys. Rev. B* **2020,** *102* (20), 205139.

51. Gao, B.; Hartland, G.; Fang, T.; Kelly, M.; Jena, D.; Xing, H.; Huang, L., Studies of Intrinsic Hot Phonon Dynamics in Suspended Graphene by Transient Absorption Microscopy. *Nano Lett.* **2011,** *11* (8), 3184-3189.

52. Cui, Q.; Ceballos, F.; Kumar, N.; Zhao, H., Transient Absorption Microscopy of Monolayer and Bulk WSe2. *ACS Nano* **2014,** *8* (3), 2970-2976.

53. Li, Y.; Shi, J.; Mi, Y.; Sui, X.; Xu, H.; Liu, X., Ultrafast carrier dynamics in two-dimensional transition metal dichalcogenides. *J. Mater. Chem. C* **2019,** *7* (15), 4304-4319.

54. T. J. Kippenberg, R. Holzwarth, and S. A. Diddams, "Microresonator-Based Optical Frequency Combs," Science, vol. 332, no. 6029, pp. 555-559, 2011.

55. L. Razzari, D. Duchesne, M. Ferrera, R. Morandotti, S. Chu, B. E. Little, and D. J. Moss, "CMOS-compatible integrated optical hyper-parametric oscillator," Nature Photonics, vol. 4, no. 1, pp. 41-45, 2010/01/01, 2010.

56. A. Pasquazi, M. Peccianti, L. Razzari, D. J. Moss, S. Coen, M. Erkintalo, Y. K. Chembo, T. Hansson, S. Wabnitz, P. Del'Haye, X. Xue, A. M. Weiner, and R. Morandotti, "Micro-combs: A novel generation of optical sources," Physics Reports, vol. 729, pp. 1-81, 2018/01/27/, 2018.

57. D. Moss, R. Morandotti, A. Gaeta, and M. Lipson, "New CMOS-compatible platforms based on silicon nitride and Hydex for nonlinear optics," Nat. Photonics, vol. 7, no. 8, pp. 597-607, Aug. 2013.

58. M. Ferrera et al., "Low-power continuous-wave nonlinear optics in doped silica glass integrated waveguide structures," Nat. photonics, vol. 2, no. 12, pp. 737-740, Dec. 2008.

59. H. Bao, A. Cooper, M. Rowley, L. Di Lauro, J. S. Totero Gongora, S. T. Chu, B. E. Little, G.-L. Oppo, R. Morandotti, D. J. Moss, B. Wetzel, M. Peccianti, and A. Pasquazi, "Laser cavity-soliton microcombs," Nature Photonics, vol. 13, no. 6, pp. 384-389, 2019/06/01, 2019.

60. M. Peccianti, A. Pasquazi, Y. Park, B. E. Little, S. T. Chu, D. J. Moss, and R. Morandotti, "Demonstration of a stable ultrafast laser based on a nonlinear microcavity," Nature Communications, vol. 3, no. 1, pp. 765, 2012/04/03, 2012.

61. L. Di Lauro, J. Li, D. J. Moss, R. Morandotti, S. T. Chu, M. Peccianti, and A. Pasquazi, "Parametric control of thermal self-pulsation in micro-cavities," Optics Letters, vol. 42, no. 17, pp. 3407-3410, 2017/09/01, 2017.

62. H. Bao, A. Cooper, S. T. Chu, D. J. Moss, R. Morandotti, B. E. Little, M. Peccianti, and A. Pasquazi, "Type-II micro-comb generation in a filter-driven four wave mixing laser [Invited]," Photonics Research, vol. 6, no. 5, pp. B67-B73, 2018/05/01, 2018.

63. A. Pasquazi et al., "Stable, dual mode, high repetition rate mode-locked laser based on a microring resonator," Optics Express, vol. 20, no. 24, pp. 27355-27363, 2012/11/19, 2012.

64. A. Pasquazi, L. Caspani, M. Peccianti, M. Clerici, M. Ferrera, L. Razzari, D. Duchesne, B. E. Little, S. T. Chu, D. J. Moss, and R. Morandotti, "Self-locked optical parametric oscillation in a CMOS compatible microring resonator: a route to robust optical frequency comb generation on a chip," Optics Express, vol. 21, no. 11, pp. 13333-13341, 2013.

65. A. Pasquazi, et al., "Sub-picosecond phase-sensitive optical pulse characterization on a chip", Nature Photonics, vol. 5, no. 10, pp. 618-623 (2011).

66. H Bao et al. "Turing patterns in a fiber laser with a nested microresonator: Robust and controllable microcomb generation", Physical Review Research vol. 2 (2), 023395 (2020).

67. M. Ferrera et al., "Low Power CW Parametric Mixing in a Low Dispersion High Index Doped Silica Glass Micro-Ring Resonator with Q-factor > 1 Million", Optics Express, vol.17, no. 16, pp. 14098–14103 (2009).

68. A. Pasquazi, Y. Park, J. Azaña, F. Légaré, R. Morandotti, B. E. Little, S. T. Chu, and D. J. Moss, "Efficient wavelength conversion and net parametric gain via Four Wave Mixing in a high index doped silica waveguide," Optics Express, vol. 18, no. 8, pp. 7634-7641, 2010/04/12, 2010.

69. A. Pasquazi, et al., "All-optical wavelength conversion in an integrated ring resonator," Optics Express, vol. 18 (4) 3858 (2010).

70. M. Peccianti, M. Ferrera, L. Razzari, et al., "Subpicosecond optical pulse compression via an integrated nonlinear chirper," Optics Express, vol. 18, no. 8, pp. 7625-7633, 2010.

71. M. Kues, et al., "Passively modelocked laser with an ultra-narrow spectral width", Nature Photonics, vol. 11, no. 3, pp. 159, 2017.

72. B. Corcoran, et al., "Ultra-dense optical data transmission over standard fiber with a single chip source", Nature Communications, vol. 11, Article:2568, 2020.

73. C.Prayoonyong et al., "Frequency comb distillation for optical superchannel transmission", Journal of Lightwave Technology Vol. 39 (23) 7383-7392 (2021).

74. X. Xu, M. Tan, B. Corcoran, J. Wu, A. Boes, T. G. Nguyen, S. T. Chu, B. E. Little, D. G. Hicks, R. Morandotti, A. Mitchell, and D. J. Moss, "11 TOPS photonic convolutional accelerator for optical neural networks," Nature, vol. 589, no. 7840, pp. 44-51, 2021/01/01, 2021.

75. W. Wang, Z. Lu, W. Zhang, S. T. Chu, B. E. Little, L. Wang, X. Xie, M. Liu, Q. Yang, L. Wang, J. Zhao, G. Wang, Q. Sun, Y. Liu, Y. Wang, and W. Zhao, "Robust soliton crystals in a thermally controlled microresonator," Optics Letters, vol. 43, no. 9, pp. 2002-2005, 2018/05/01, 2018.

76. D. C. Cole, E. S. Lamb, P. Del'Haye, S. A. Diddams, and S. B. Papp, "Soliton crystals in Kerr resonators," Nature Photonics, vol. 11, no. 10, pp. 671-676, 2017/10/01, 2017.

77. M. Karpov, M. H. P. Pfeiffer, H. Guo, W. Weng, J. Liu, and T. J. Kippenberg, "Dynamics of soliton crystals in optical microresonators," Nature Physics, vol. 15, no. 10, pp. 1071-1077, 2019/10/01, 2019.

78. V. Torres-Company, and A. M. Weiner, “Optical frequency comb technology for ultra-broadband radio-frequency photonics,” Laser & Photonics Reviews, vol. 8, no. 3, pp. 368-393, 2014.

79. Chou, J., Han, Y., and Jalali, B.: ‘Adaptive RF-photonic arbitrary waveform generator’, IEEE Photonics Technology Letters, 2003, 15, (4), pp. 581-583

80. X. Xue, Y. Xuan, H.-J. Kim, J. Wang, D. E. Leaird, M. Qi, and A. M. Weiner, “Programmable Single-Bandpass Photonic RF Filter Based on Kerr Comb from a Microring,” Journal of Lightwave Technology, vol. 32, no. 20, pp. 3557-3565, 2014/10/15, 2014.

81. X. Xu, J. Wu, M. Shoeiby, T. G. Nguyen, S. T. Chu, B. E. Little, R. Morandotti, A. Mitchell, and D. J. Moss, “Reconfigurable broadband microwave photonic intensity differentiator based on an integrated optical frequency comb source,” APL Photonics, vol. 2, no. 9, pp. 096104, 2017.

82. X. Xu, M. Tan, J. Wu, R. Morandotti, A. Mitchell, and D. J. Moss, “Microcomb-Based Photonic RF Signal Processing,” IEEE Photonics Technology Letters, vol. 31, no. 23, pp. 1854-1857, 2019.

83. X. Xue, Y. Xuan, C. Bao, S. Li, X. Zheng, B. Zhou, M. Qi, and A. M. Weiner, “Microcomb-Based True-Time-Delay Network for Microwave Beamforming With Arbitrary Beam Pattern Control,” Journal of Lightwave Technology, vol. 36, no. 12, pp. 2312-2321, 2018.

84. X. Xu, J. Wu, T. G. Nguyen, S. T. Chu, B. E. Little, R. Morandotti, A. Mitchell, and D. J. Moss, “Broadband RF Channelizer Based on an Integrated Optical Frequency Kerr Comb Source,” Journal of Lightwave Technology, vol. 36, no. 19, pp. 4519-4526, 2018.

85. X. Xu, J. Wu, M. Tan, T. G. Nguyen, S. T. Chu, B. E. Little, R. Morandotti, A. Mitchell, and D. J. Moss, “Orthogonally Polarized RF Optical Single Sideband Generation and Dual-Channel Equalization Based on an Integrated Microring Resonator,” Journal of Lightwave Technology, vol. 36, no. 20, pp. 4808-4818, 2018.

86. X. Xu, M. Tan, J. Wu, T. G. Nguyen, S. T. Chu, B. E. Little, R. Morandotti, A. Mitchell, and D. J. Moss, “Advanced Adaptive Photonic RF Filters with 80 Taps Based on an Integrated Optical Micro-Comb Source,” Journal of Lightwave Technology, vol. 37, no. 4, pp. 1288-1295, 2019/02/15, 2019.

87. W. Liang, D. Eliyahu, V. S. Ilchenko, A. A. Savchenkov, A. B. Matsko, D. Seidel, and L. Maleki, “High spectral purity Kerr frequency comb radio frequency photonic oscillator,” Nature Communications, vol. 6, no. 1, pp. 7957, 2015/08/11, 2015.

88. J. Liu, E. Lucas, A. S. Raja, J. He, J. Riemensberger, R. N. Wang, M. Karpov, H. Guo, R. Bouchand, and T. J. Kippenberg, “Photonic microwave generation in the X- and K-band using integrated soliton microcombs,” Nature Photonics, vol. 14, no. 8, pp. 486-491, 2020/08/01, 2020.

89. M. Tan, X. Xu, J. Wu, R. Morandotti, A. Mitchell, and D. J. Moss, “Photonic RF and microwave filters based on 49 GHz and 200 GHz Kerr microcombs,” Optics Communications, vol. 465, pp. 125563, 2020/06/15/, 2020.

90. X. Xu, M. Tan, J. Wu, A. Boes, T. G. Nguyen, S. T. Chu, B. E. Little, R. Morandotti, A. Mitchell, and D. J. Moss, “Broadband Photonic RF Channelizer With 90 Channels Based on a Soliton Crystal Microcomb,” Journal of Lightwave Technology, vol. 38, no. 18, pp. 5116-5121, 2020.

91. X. Xu, M. Tan, J. Wu, A. Boes, B. Corcoran, T. G. Nguyen, S. T. Chu, B. E. Little, R. Morandotti, A. Mitchell, and D. Moss, “Photonic RF Phase-Encoded Signal Generation With a Microcomb Source,” Journal of Lightwave Technology, vol. 38, no. 7, pp. 1722-1727, 2020.

92. X. Xu, M. Tan, J. Wu, T. G. Nguyen, S. T. Chu, B. E. Little, R. Morandotti, A. Mitchell, and D. J. Moss, “High performance RF filters via bandwidth scaling with Kerr micro-combs,” APL Photonics, vol. 4, no. 2, pp. 026102, 2019.

93. M. Tan, X. Xu, B. Corcoran, J. Wu, A. Boes, T. G. Nguyen, S. T. Chu, B. E. Little, R. Morandotti, A. Mitchell, and D. J. Moss, “Microwave and RF Photonic Fractional Hilbert Transformer Based on a 50 GHz Kerr Micro-Comb,” Journal of Lightwave Technology, vol. 37, no. 24, pp. 6097-6104, 2019.

94. M. Tan, X. Xu, B. Corcoran, J. Wu, A. Boes, T. G. Nguyen, S. T. Chu, B. E. Little, R. Morandotti, A. Mitchell, and D. J. Moss, “RF and Microwave Fractional Differentiator Based on Photonics,” IEEE Transactions on Circuits and Systems II: Express Briefs, vol. 67, no. 11, pp. 2767-2771, 2020.

95. M. Tan, X. Xu, A. Boes, B. Corcoran, J. Wu, T. G. Nguyen, S. T. Chu, B. E. Little, R. Morandotti, A. Mitchell, and D. J. Moss, "Photonic RF Arbitrary Waveform Generator Based on a Soliton Crystal Micro-Comb Source," Journal of Lightwave Technology, vol. 38, no. 22, pp. 6221-6226, 2020/11/15, 2020.

96. M. Tan, X. Xu, J. Wu, R. Morandotti, A. Mitchell, and D. Moss, "RF and microwave photonic temporal signal processing with Kerr micro-combs," Advances in Physics: X, vol. 6, no. 1, pp. 1-46, 2021.

97. Mengxi Tan, Xingyuan Xu, Jiayang Wu, Bill Corcoran, Andreas Boes, Thach G. Nguyen, Sai T. Chu, Brent E. Little, Roberto Morandotti, Arnan Mitchell, and David J. Moss, "Integral order photonic RF signal processors based on a soliton crystal micro-comb source", IOP Journal of Optics Vol. 23 (11) 125701 (2021).

98. M. Tan, X. Xu, J. Wu, T. G. Nguyen, S. T. Chu, B. E. Little, R. Morandotti, A. Mitchell, and D. J. Moss, "Photonic Radio Frequency Channelizers based on Kerr Optical Micro-combs", IOP Journal of Semiconductors Vol. 42 (4), 041302 (2021).

99. M. Tan, X. Xu, J. Wu, T. G. Nguyen, S. T. Chu, B. E. Little, R. Morandotti, A. Mitchell, and D. J. Moss, "Orthogonally polarized Photonic Radio Frequency single sideband generation with integrated micro-ring resonators", IOP Journal of Semiconductors, Vol. 42 (4), 041305 (2021).

100. T. G. Nguyen et al., "Integrated frequency comb source-based Hilbert transformer for wideband microwave photonic phase analysis," Opt. Express, vol. 23, no. 17, pp. 22087-22097, Aug. 2015.

101. X. Xu, et al., "Continuously tunable orthogonally polarized RF optical single sideband generator based on micro-ring resonators," Journal of Optics, vol. 20, no. 11, 115701. 2018.

102. M. Tan, X. Xu, J. Wu, A. Boes, B. Corcoran, T. G. Nguyen, S. T. Chu, B. E. Little, R. Morandotti, A. Mitchell, and D. J. Moss, "Advanced applications of Kerr mircocombs", Paper 11775-1. SPIE 11775, Integrated Optics: Design, Devices, Systems and Applications VI, (EOO21) OO107-8, Proc 1177504 (18 April 2021); Integrated Optics Conference, SPIE Optics and Optoelectronics Symposium, Prague, Czech Republic. April 19 - 22 (2021), doi.org/10.1117/12.2588733.

103. X. Xu, et al., Broadband microwave frequency conversion based on an integrated optical micro-comb source", Journal of Lightwave Technology, vol. 38 no. 2, pp. 332-338, 2020.

104. X. Xu, et al., "Photonic RF and microwave integrator with soliton crystal microcombs", IEEE Transactions on Circuits and Systems II: Express Briefs, vol. 67, no. 12, pp. 3582-3586, 2020.

105. M. Tan, X. Xu, J. Wu, R. Morandotti, A. Mitchell, and D. J. Moss, "RF and microwave high bandwidth signal processing based on Kerr Micro-combs", Advances in Physics X, VOL. 6, NO. 1, 1838946 (2021).

106. M. Tan, X. Xu, J. Wu, B. Corcoran, A. Boes, T. G. Nguyen, S. T. Chu, B. E. Little, R.Morandotti, A. Lowery, A. Mitchell, and D. J. Moss, ""'Highly Versatile Broadband RF Photonic Fractional Hilbert Transformer Based on a Kerr Soliton Crystal Microcomb", Journal of Lightwave Technology vol. 39 (24) 7581-7587 (2021).

107. L. Moura, "Radio Frequency Implementation of the Fractional Hilbert Transform with Transversal Filters," Circuits, Systems & Signal Processing, vol. 26, pp. 407-417, 2007.

108. A. W. Lohmann, D. Mendlovic, and Z. Zalevsky, "Fractional Hilbert transform," Optics Letters, vol. 21, no. 4, pp. 281-283, 1996/02/15, 1996.

109. A. D. Poularikas, A. F. Poularikas, and P. A. D, The Transforms and Applications Handbook: CRC-Press, 1996.

110. V. K. Peddinti, and R. Kumaresan, "Bandpass phase shifter and analytic signal generator," Signal Process., vol. 125, no. C, pp. 216–220, 2016.

111. H. P. Bazargani, M. d. R. Fernández-Ruiz, and J. Azaña, "Tunable, nondispersive optical filter using photonic Hilbert transformation," Optics Letters, vol. 39, no. 17, pp. 5232-5235, 2014/09/01, 2014.

112. H. P. Bazargani, M. R. Fernández-Ruiz, and J. Azaña, "Tunable optical filter using photonic Hilbert transformation," OSA Technical Digest (online). p. SPM4D.6.

113. H. Emami, N. Sarkhosh, L. A. Bui, and A. Mitchell, "Wideband RF photonic in-phase and quadrature-phase generation," Optics Letters, vol. 33, no. 2, pp. 98-100, 2008/01/15, 2008.

114. M. Li, and J. Yao, "All-fiber temporal photonic fractional Hilbert transformer based on a directly designed fiber Bragg grating," Optics Letters, vol. 35, no. 2, pp. 223-225, 2010/01/15, 2010.

115. M. Li, and J. Yao, "Experimental Demonstration of a Wideband Photonic Temporal Hilbert Transformer Based on a Single Fiber Bragg Grating," IEEE Photonics Technology Letters, vol. 22, no. 21, pp. 1559-1561, 2010.
116. M. H. Asghari, and J. Azaña, "All-optical Hilbert transformer based on a single phase-shifted fiber Bragg grating: design and analysis," Optics Letters, vol. 34, no. 3, pp. 334-336, 2009/02/01, 2009.
117. T. Yang, J. Dong, L. Liu, S. Liao, S. Tan, L. Shi, D. Gao, and X. Zhang, "Experimental observation of optical differentiation and optical Hilbert transformation using a single SOI microdisk chip," Scientific Reports, vol. 4, no. 1, pp. 3960, 2014/02/04, 2014.
118. Z. Zhang, C. Sima, B. Liu, B. Cai, Y. Gao, M. Zhang, L. Shen, Y. Yu, M. Huang, Z. Lian, M. T. Posner, J. C. Gates, P. G. R. Smith, and D. Liu, "Wideband and continuously-tunable fractional photonic Hilbert transformer based on a single high-birefringence planar Bragg grating," Optics Express, vol. 26, no. 16, pp. 20450-20458, 2018/08/06, 2018.
119. C. Sima, J. C. Gates, C. Holmes, P. L. Mennea, M. N. Zervas, and P. G. R. Smith, "Terahertz bandwidth photonic Hilbert transformers based on synthesized planar Bragg grating fabrication," Optics Letters, vol. 38, no. 17, pp. 3448-3451, 2013/09/01, 2013.
120. L. Zhuang, M. R. Khan, W. Beeker, A. Leinse, R. Heideman, and C. Roeloffzen, "Novel microwave photonic fractional Hilbert transformer using a ring resonator-based optical all-pass filter," Optics Express, vol. 20, no. 24, pp. 26499-26510, 2012/11/19, 2012.
121. H. Shahoei, P. Dumais, and J. Yao, "Continuously tunable photonic fractional Hilbert transformer using a high-contrast germanium-doped silica-on-silicon microring resonator," Optics Letters, vol. 39, no. 9, pp. 2778-2781, 2014/05/01, 2014.
122. W. Liu, M. Li, R. S. Guzzon, E. J. Norberg, J. S. Parker, M. Lu, L. A. Coldren, and J. Yao, "A fully reconfigurable photonic integrated signal processor," Nature Photonics, vol. 10, no. 3, pp. 190-195, 2016/03/01, 2016.
123. Z. Li, Y. Han, H. Chi, X. Zhang, and J. Yao, "A Continuously Tunable Microwave Fractional Hilbert Transformer Based on a Nonuniformly Spaced Photonic Microwave Delay-Line Filter," Journal of Lightwave Technology, vol. 30, no. 12, pp. 1948-1953, 2012/06/15, 2012.
124. Z. Li, H. Chi, X. Zhang, and J. Yao, "A Continuously Tunable Microwave Fractional Hilbert Transformer Based on a Photonic Microwave Delay-Line Filter Using a Polarization Modulator," IEEE Photonics Technology Letters, vol. 23, no. 22, pp. 1694-1696, 2011.
125. Y. Park, M. H. Asghari, R. Helsten, and J. Azana, "Implementation of Broadband Microwave Arbitrary-Order Time Differential Operators Using a Reconfigurable Incoherent Photonic Processor," IEEE Photonics Journal, vol. 2, no. 6, pp. 1040-1050, 2010.
126. J. Feldmann, N. Youngblood, M. Karpov, H. Gehring, X. Li, M. Stappers, M. Le Gallo, X. Fu, A. Lukashchuk, A. S. Raja, J. Liu, C. D. Wright, A. Sebastian, T. J. Kippenberg, W. H. P. Pernice, and H. Bhaskaran, "Parallel convolutional processing using an integrated photonic tensor core," Nature, vol. 589, no. 7840, pp. 52-58, 2021/01/01, 2021.
127. D. Marpaung, J. Yao, and J. Capmany, "Integrated microwave photonics," Nature Photonics, vol. 13, no. 2, pp. 80-90, 2019/02/01, 2019.
128. Z. Zhu, H. Chi, T. Jin, S. Zheng, X. Jin, and X. Zhang, "All-positive-coefficient microwave photonic filter with rectangular response," Optics Letters, vol. 42, no. 15, pp. 3012-3015, 2017/08/01, 2017.
129. R. A. Minasian, "Ultra-Wideband and Adaptive Photonic Signal Processing of Microwave Signals," IEEE Journal of Quantum Electronics, vol. 52, no. 1, pp. 1-13, 2016.
130. W. Wang, W. Zhang, Z. Lu, S. T. Chu, B. E. Little, Q. Yang, L. Wang, and W. Zhao, "Self-locked orthogonal polarized dual comb in a microresonator," Photonics Research, vol. 6, no. 5, pp. 363-367, 2018/05/01, 2018.
131. J. Capmany, J. Mora, I. Gasulla, J. Sancho, J. Lloret, and S. Sales, "Microwave Photonic Signal Processing," Journal of Lightwave Technology, vol. 31, no. 4, pp. 571-586, 2013/02/15, 2013.
132. R. A. Minasian, "Photonic signal processing of microwave signals," IEEE Transactions on Microwave Theory and Techniques, vol. 54, no. 2, pp. 832-846, 2006.
133. J. Capmany, and D. Novak, "Microwave photonics combines two worlds," Nature Photonics, vol. 1, no. 6, pp. 319-330, 2007/06/01, 2007.
134. R. Williamson, and R. D. Esman, "RF Photonics," Journal of Lightwave Technology, vol. 26, no. 9, pp. 1145-1153, 2008/05/01, 2008.
135. Y. Liu, J. Hotten, A. Choudhary, B. J. Eggleton, and D. Marpaung, "All-optimized integrated RF photonic notch filter," Optics Letters, vol. 42, no. 22, pp. 4631-4634, 2017/11/15, 2017.

136. C. Tseng, and S.-C. Pei, “Design and application of discrete-time fractional Hilbert transformer,” Circuits and Systems II: Analog and Digital Signal Processing, IEEE Transactions on, vol. 47, pp. 1529-1533, 01/01, 2001.
137. J. A. Davis, D. E. McNamara, and D. M. Cottrell, “Analysis of the fractional Hilbert transform,” Appl. Opt., vol. 37, no. 29, pp. 6911-6913, Oct. 1998.
138. C. D. Holdenried, J. W. Haslett, and B. Davies, “A fully integrated 10-Gb/s tapped delay Hilbert transformer for optical single sideband,” IEEE Microw. Wireless Compon. Lett., vol. 15, no. 5, pp. 303-305, May 2005.
139. H. Emami, N. Sarkhosh, L. A. Bui, and A. Mitchell, “Wideband RF photonic in-phase and quadrature-phase generation,” Opt. Lett., vol. 33, no. 2, pp. 98-100, Jan 15. 2008.
140. W. Liu, et al., "A Fully Reconfigurable Photonic Integrated Signal Processor," Nature Photonics, vol. 10, no. 3, pp. 190-196, 2016.
141. F. Zeng, and J. Yao, “An Approach to Ultrawideband Pulse Generation and Distribution Over Optical Fiber,” IEEE Photonics Technol. Lett., vol. 18, no. 7, pp. 823-825, Apr. 2006.
142. S. Pan, and J. Yao, “Optical generation of polarity- and shape-switchable ultrawideband pulses using a chirped intensity modulator and a first-order asymmetric Mach-Zehnder interferometer,” Opt. Lett., vol. 34, no. 9, pp. 1312-1314, May. 2009.
143. Y. Yu, J. Dong, X. Li, and X. Zhang, “Ultra-Wideband Generation Based on Cascaded Mach-Zehnder Modulators,” IEEE Photonics Technol. Lett., vol. 23, no. 23, Dec. 2011.
144. A. O.-Blanch, J. Mora, J. Capmany, B. Ortega, and D. Pastor, “Tunable radio-frequency photonic filter based on an actively mode-locked fiber laser,” Opt. Lett., vol. 31, no. 6, pp. 709-711, Mar. 2006.
145. V. R. Supradeepa, C. M. Long, R. Wu. F. Ferdous, E. Hamidi, D. E. Leaird, and A. M. Weiner, “Comb-based radiofrequency photonic filters with rapid tunability and high selectivity,” Nature Photonics, vol. 6, pp. 186-194, Mar. 2012.
146. V. T.-Company, and A. M. Weiner, “Optical frequency comb technology for ultra-broadband radio-frequency photonics,” Laser Photonics Rev., vol. 8, no. 3, pp. 368-393, 2014.
147. Ghelfi, P., Laghezza, F., Scotti, F., Serafino, G., Capria, A., Pinna, S., Onori, D., Porzi, C., Scaffardi, M., Malacarne, A., Vercesi, V., Lazzeri, E., Berizzi, F., and Bogoni, A.: ‘A fully photonics-based coherent radar system’, Nature, 2014, 507, (7492), pp. 341-345
148. Skolnik, M.: ‘Role of radar in microwaves’, IEEE Transactions on Microwave Theory and Techniques, 2002, 50, (3), pp. 625-632
149. Cundiff, S.T., and Weiner, A.M.: ‘Optical arbitrary waveform generation’, Nat. Photonics, 2010, 4, (11), pp. 760-766
150. Rashidinejad, A., Li, Y., and Weiner, A.M.: ‘Recent Advances in Programmable Photonic-Assisted Ultrabroadband Radio-Frequency Arbitrary Waveform Generation’, IEEE Journal of Quantum Electronics, 2016, 52, (1), pp. 1-17
151. Ghelfi, P., Scotti, F., Laghezza, F., and Bogoni, A.: ‘Photonic Generation of Phase-Modulated RF Signals for Pulse Compression Techniques in Coherent Radars’, Journal of Lightwave Technology, 2012, 30, (11), pp. 1638-1644
152. Khan, M.H., Shen, H., Xuan, Y., Zhao, L., Xiao, S., Leaird, D.E., Weiner, A.M., and Qi, M.: ‘Ultrabroad-bandwidth arbitrary radiofrequency waveform generation with a silicon photonic chip-based spectral shaper’, Nat. Photonics, 2010, 4, (2), pp. 117-122
153. Chi, H., and Yao, J.: ‘Photonic Generation of Phase-Coded Millimeter-Wave Signal Using a Polarization Modulator’, IEEE Microwave and Wireless Components Letters, 2008, 18, (5), pp. 371-373
154. Zhang, Y., and Pan, S.: ‘Generation of phase-coded microwave signals using a polarization-modulator-based photonic microwave phase shifter’, Opt. Lett., 2013, 38, (5), pp. 766-768
155. Zhu, S., Shi, Z., Li, M., Zhu, N.H., and Li, W.: ‘Simultaneous frequency upconversion and phase coding of a radio-frequency signal for photonic radars’, Opt. Lett., 2018, 43, (3), pp. 583-586
156. Zhu, S., Li, M., Wang, X., Zhu, N.H., Cao, Z.Z., and Li, W.: ‘Photonic generation of background-free binary phase-coded microwave pulses’, Opt. Lett., 2019, 44, (1), pp. 94-97
157. Li, Z., Li, W., Chi, H., Zhang, X., and Yao, J.: ‘Photonic generation of phase-coded microwave signal with large frequency tunability’, IEEE Photonics Technology Letters, 2011, 23, (11), pp. 712-714
158. Liu, W., and Yao, J.: ‘Photonic generation of microwave waveforms based on a polarization modulator in a Sagnac loop’, Journal of Lightwave Technology, 2014, 32, (20), pp. 3637-3644

159. Wang, J., Shen, H., Fan, L., Wu, R., Niu, B., Varghese, L.T., Xuan, Y., Leaird, D.E., Wang, X., and Gan, F.: 'Reconfigurable radio-frequency arbitrary waveforms synthesized in a silicon photonic chip', Nat. Commun., 2015, 6, (1), pp. 1-8
160. Ashrafi, R., Li, M., and Azaña, J.: 'Multi-TBaud optical coding based on superluminal space-to-time mapping in long period gratings', Optics and Photonics Journal, 2013, 3, (2), pp. 126-130
161. Rashidinejad, A., and Weiner, A.M.: 'Photonic radio-frequency arbitrary waveform generation with maximal time-bandwidth product capability', Journal of Lightwave Technology, 2014, 32, (20), pp. 3383-3393
162. Jiang, Z., Huang, C.-B., Leaird, D.E., and Weiner, A.M.: 'Optical arbitrary waveform processing of more than 100 spectral comb lines', Nat. Photonics, 2007, 1, (8), pp. 463-467
163. Dai, Y., and Yao, J.: 'Microwave pulse phase encoding using a photonic microwave delay-line filter', Opt. Lett., 2007, 32, (24), pp. 3486-3488
164. S. Pan, J. Yao, "Optical generation of polarity- and shape-switchable ultrawideband pulses using a chirped intensity modulator and a first-order asymmetric Mach-Zehnder interferometer," Opt. Lett., vol. 34, no. 9, pp. 1312-1314, 2009.
165. X. Li, J. Dong, Y. Yu, and X. Zhang, "A Tunable Microwave Photonic Filter Based on an All-Optical Differentiator," IEEE Photon. Technol. Lett., vol. 23, no. 22, pp. 308-310, Mar. 2011.
166. Y. Han, Z. Li, and J. Yao, "A Microwave Bandpass Differentiator Implemented Based on a Nonuniformly-Spaced Photonic Microwave Delay-Line Filter," J. Lightw. Technol., vol. 29, no. 22, pp. 3470-3475, Nov. 2011.
167. R. Ashrafi and J. Azaña, "Figure of merit for photonic differentiators," Opt. Exp., vol. 20, no. 3, pp. 2626-2639, Jan. 2012.
168. F. Zeng and J. Yao, "Ultrawideband Impulse Radio Signal Generation Using a High-Speed Electrooptic Phase Modulator and a Fiber-Bragg-Grating-Based Frequency Discriminator," IEEE Photon. Technol. Lett., vol. 18, no. 19, pp. 2062-2064, Oct. 2006.
169. P. Li, H. Chen, M. Chen, and S. Xie, "Gigabit/s Photonic Generation, Modulation, and Transmission for a Reconfigurable Impulse Radio UWB Over Fiber System," IEEE Photon. Technol. Lett., vol. 4, no. 3, pp. 805-816, Jun. 2012.
170. Y. Yu, F. Jiang, H. Tang, L. Xu, X. Liu, J. Dong, and X. Zhang, "Reconfigurable photonic temporal differentiator based on a dual-drive Mach-Zehnder modulator," Opt. Exp., vol. 24, no. 11, pp. 11739-11748, May 2016.
171. P. Velanas, A. Bogris, A. Argyris, and D. Syvridis, "High-Speed All-Optical First- and Second-Order Differentiators Based on Cross-Phase Modulation in Fibers," J. Lightw. Technol., vol. 26, no. 18, pp. 3269-3276, Sep. 2008.
172. J. Xu, X. Zhang, J. Dong, D. Liu, and D. Huang, "All-optical differentiator based on cross-gain modulation in semiconductor optical amplifier," Opt. Lett., vol. 32, no. 20, pp. 3029-3031, Oct. 2007.
173. J. Xu, X. Zhang, J. Dong, D. Liu, and D. Huang, "High-speed all-optical differentiator based on a semiconductor optical amplifier and an optical filter," Opt. Lett., vol. 32, no. 13, pp. 1872-1874, Jul. 2007.
174. F. Wang, J. Dong, E. Xu, and X. Zhang, "All-optical UWB generation and modulation using SOA-XPM effect and DWDM-based multi-channel frequency discrimination," Opt. Exp., vol. 18, no. 24, pp. 24588-24594, Nov. 2010.
175. V. Moreno, M. Rius, J. Mora, M. A. Muriel, and J. Capmany, "Integrable high order UWB pulse photonic generator based on cross phase modulation in a SOA-MZI," Opt. Exp., vol. 21, no. 19, pp. 22911-22917, Sep. 2013.
176. Q. Wang and J. Yao, "Switchable optical UWB monocycle and doublet generation using a reconfigurable photonic microwave delay-line filter," Opt. Exp., vol. 15, no. 22, pp. 14667-14672, Oct. 2007.
177. M. Bolea, J. Mora, B. Ortega, and J. Capmany, "Optical UWB pulse generator using an N tap microwave photonic filter and phase inversion adaptable to different pulse modulation formats," Opt. Exp., vol. 17, no. 7, pp. 5023-50332, Mar. 2009.
178. B. Mathieu, P. Melchior, A. Oustaloup, C. Ceyral, "Fractional differentiation for edge detection," Signal Processing, vol. 83, pp. 2421-2432, Nov. 2003.
179. A. Oustaloup, F. Levron, B. Mathieu, and F. M. Nanot, "Frequency-Band Complex Noninteger Differentiator: Characterization and Synthesis," IEEE Trans. on Circuit and Systems - I: Fundamental Theory and Application, vol. 47, no. 1, pp. 25-39, Jan. 2000.

180. F. Li, Y. Park, and J. Azaña, "Linear Characterization of Optical Pulses With Durations Ranging From the Picosecond to the Nanosecond Regime Using Ultrafast Photonic Differentiation," J. Lightw. Technol., vol. 27, no. 1, pp. 4623-4633, 2009.
181. Stern, B., Ji, X., Okawachi, Y., Gaeta, A. L. & Lipson, M. Battery-operated integrated frequency comb generator. Nature 562, 401 (2018).
182. W. Wang, Z. Lu, W. Zhang, S. T. Chu, B. E. Little, L. Wang, X. Xie, M. Liu, Q. Yang, L. Wang, J. Zhao, G. Wang, Q. Sun, Y. Liu, Y. Wang, and W. Zhao, "Robust soliton crystals in a thermally controlled microresonator," Optics Letters, vol. 43, no. 9, pp. 2002-2005, 2018/05/01, 2018.
183. D. C. Cole, E. S. Lamb, P. Del'Haye, S. A. Diddams, and S. B. Papp, "Soliton crystals in Kerr resonators," Nature Photonics, vol. 11, no. 10, pp. 671-676, 2017/10/01, 2017.
184. M. Karpov, M. H. P. Pfeiffer, H. Guo, W. Weng, J. Liu, and T. J. Kippenberg, "Dynamics of soliton crystals in optical microresonators," Nature Physics, vol. 15, no. 10, pp. 1071-1077, 2019/10/01, 2019.
185. V. Torres-Company, and A. M. Weiner, "Optical frequency comb technology for ultra-broadband radio-frequency photonics," Laser & Photonics Reviews, vol. 8, no. 3, pp. 368-393, 2014.
186. Chou, J., Han, Y., and Jalali, B.: 'Adaptive RF-photonic arbitrary waveform generator', IEEE Photonics Technology Letters, 2003, 15, (4), pp. 581-583
187. X. Xue, Y. Xuan, H.-J. Kim, J. Wang, D. E. Leaird, M. Qi, and A. M. Weiner, "Programmable Single-Bandpass Photonic RF Filter Based on Kerr Comb from a Microring," Journal of Lightwave Technology, vol. 32, no. 20, pp. 3557-3565, 2014/10/15, 2014.
188. T. J. Kippenberg, R. Holzwarth, and S. A. Diddams, "Microresonator-Based Optical Frequency Combs," Science, vol. 332, no. 6029, pp. 555-559, 2011.
189. W. Liang, D. Eliyahu, V. S. Ilchenko, A. A. Savchenkov, A. B. Matsko, D. Seidel, and L. Maleki, "High spectral purity Kerr frequency comb radio frequency photonic oscillator," Nature Communications, vol. 6, no. 1, pp. 7957, 2015/08/11, 2015.
190. J. Liu, E. Lucas, A. S. Raja, J. He, J. Riemensberger, R. N. Wang, M. Karpov, H. Guo, R. Bouchand, and T. J. Kippenberg, "Photonic microwave generation in the X- and K-band using integrated soliton microcombs," Nature Photonics, vol. 14, no. 8, pp. 486-491, 2020/08/01, 2020.

SUPPORTING INFORMATION

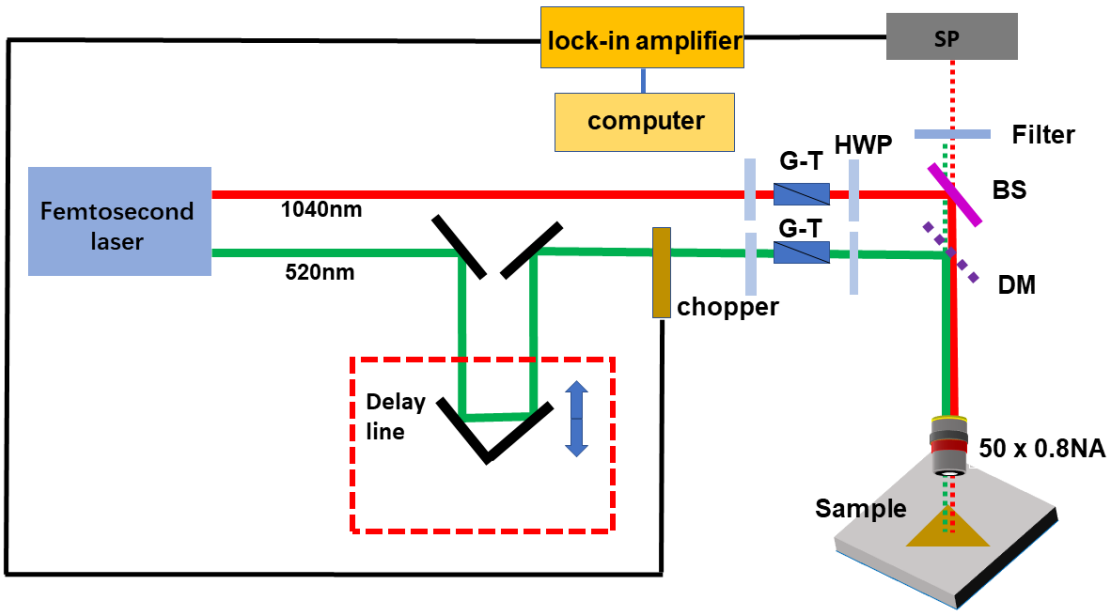

Figure S1. Schematic diagram for the time-resolved transient reflection measurement system. BS: beam-splitter; HWP: half-wave plate; DM: dichroic mirror; SP: Silicon photodiode detector; G-T: Glan-Taylor prism.

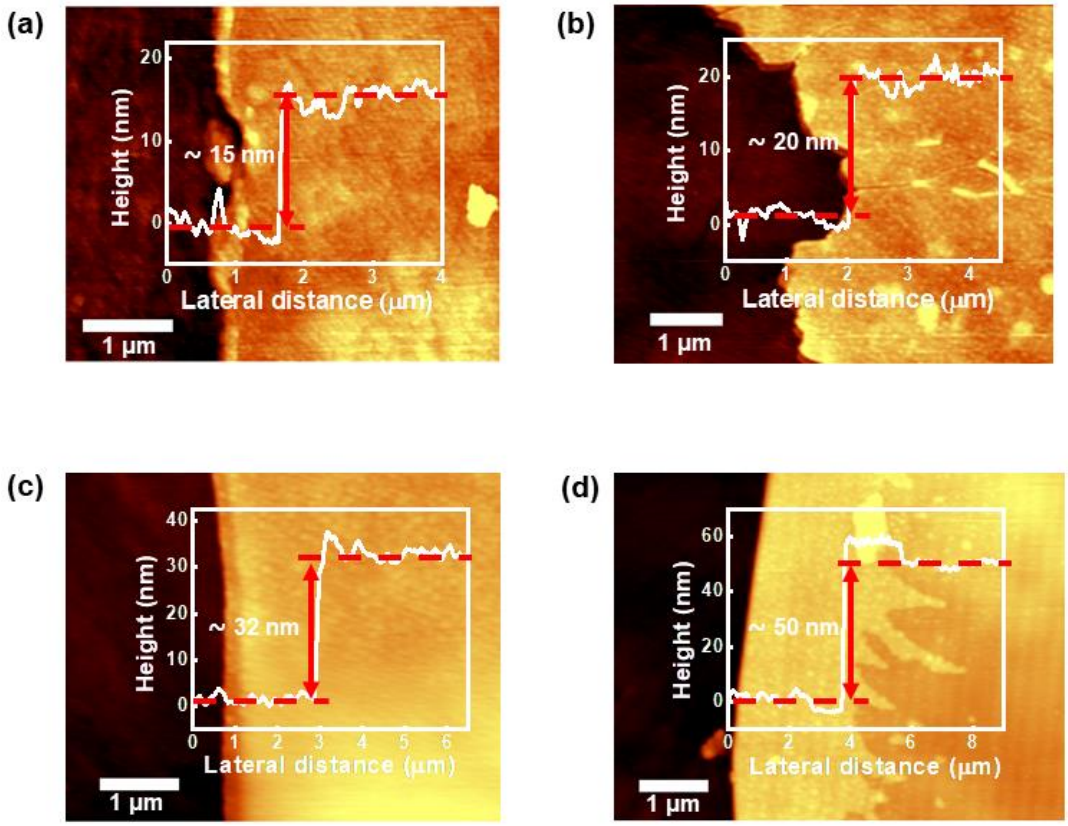

Figure S2. (a)–(d) AFM images and height profiles for $NbTe_2$ samples with different thicknesses.

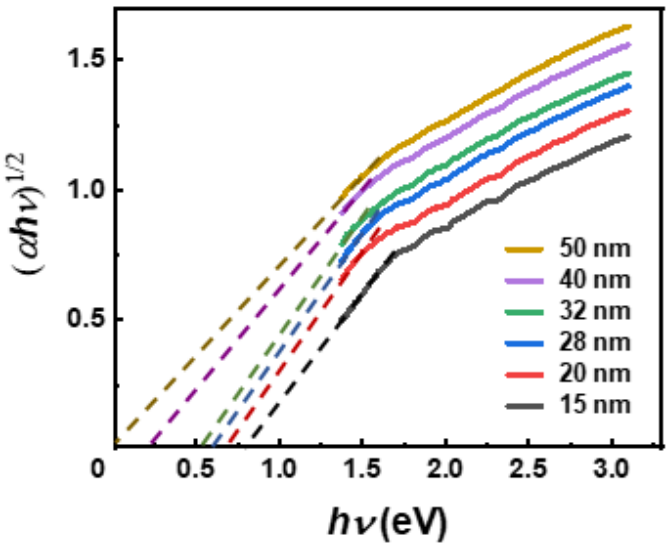

Figure S3. Tauc plots of $NbTe_2$ flakes with different thicknesses.

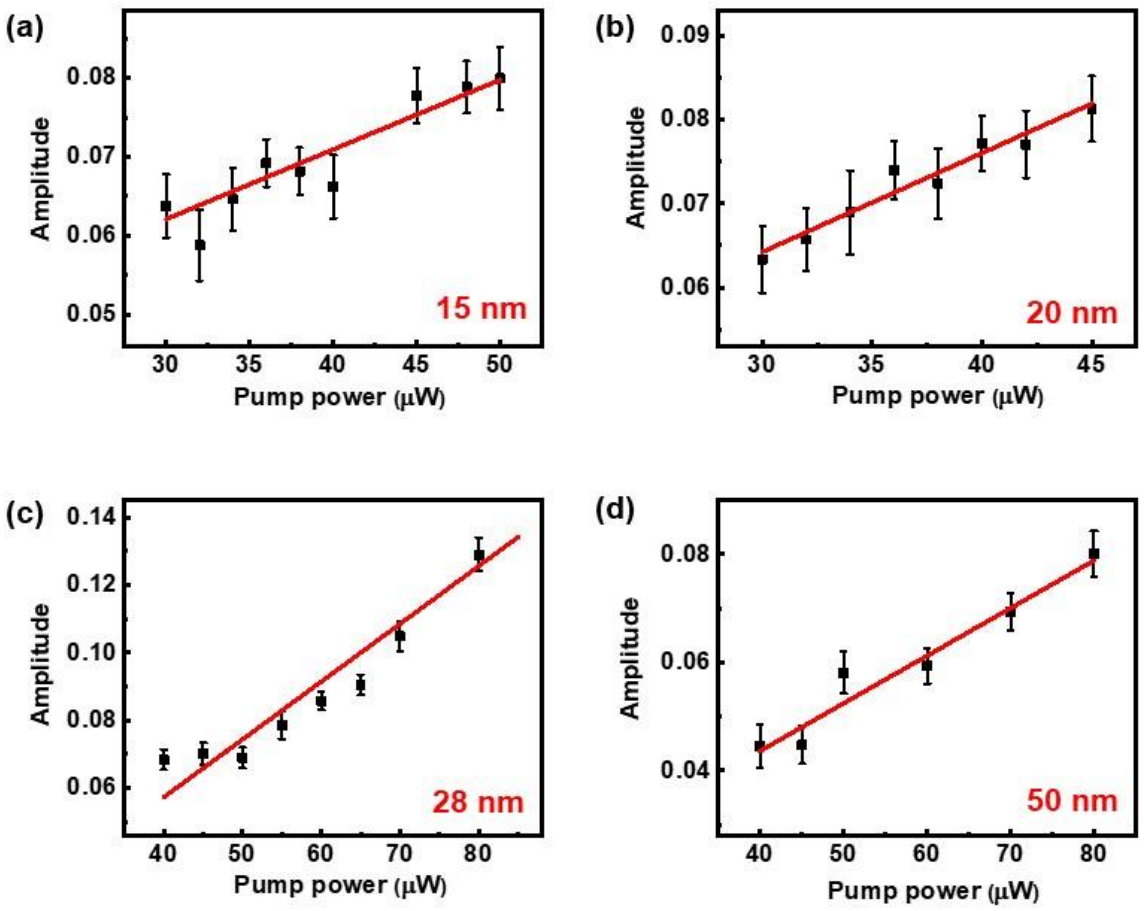

Figure S4. (a)–(d) Peak amplitudes of the ΔR curves as a function of the pump power for $NbTe_2$ flakes with different thicknesses. The black solid squares represent the experimental data, and the red solid line is the linear fit.

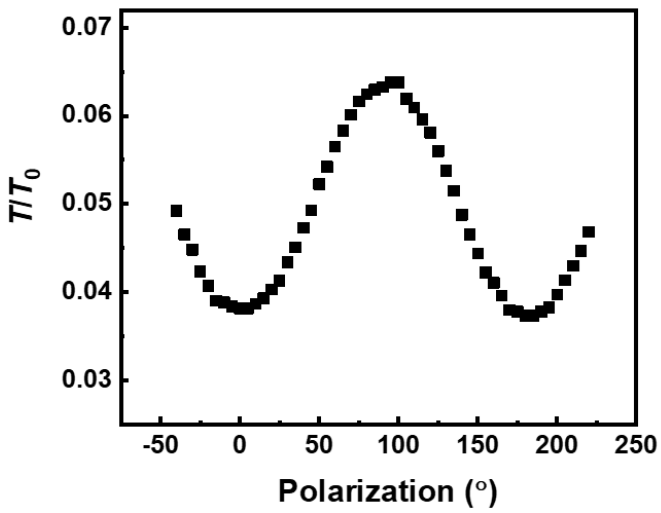

Figure S5. Polarization-resolved transmission of 520 nm pump light in $NbTe_2$ sample. T and T_0 are measured transmissions for the sample and quartz substrate, respectively.